Ultra WideBand enabled Inertial Odometry for Generic Localization

Emil Fresk, Kristoffer Ödmark, George Nikolakopoulos

Robotics Group, Department of Computer Science, Electrical and Space Engineering, Luleå University of Technology, SE–97187, Luleå, Sweden (e-mail: emil.fresk@ltu.se)

Abstract: In this paper we will present a inertial odometry localization system, utilizing Ultra WideBand distance measurements for corrections, as a generic localization solution. The proposed scheme is evaluated in two different measurement schemes, one cyclic and one based on stochastic events, which has the strong merit of minimizing the sampling rate, while adhering to covariance constraints on the state, allowing the system to conform with RF regulations. The efficacy of the proposed scheme is evaluated in extended experimental evaluation on an hexacopter Unmanned Aerial Vehicle.

Keywords: Ultra WideBand, Inertial Odometry, Localization, Error-state Kalman Filter, Stochastic event driven

1. INTRODUCTION

In the area of robotics one of the main questions, if not *the* most important one, is "*Where am I?*", a fundamental question which is the driving force in many research activities in this area, as more commonly known as the problem of localization. In the specific case of autonomous robots, generally, the localization problem sets the performance constraints of the system as the more dexterous the localization information is the more complicated and accurate the robotic tasks can be accomplished. In the ideal situations, where the robotic system can be operated with an almost perfect localization information, *e.g.* by the utilization of motion capture systems, the robotic systems can be pushed to their limits with a profound set of capabilities and autonomy levels Mellinger and Kumar (2011).

In the related literature, a plethora of localization systems have been proposed and evaluated, with characteristic works to include laser scanners Zhao et al. (2008); Newman et al. (2006) being dependent on their view of the scene, sonars Tardós et al. (2002); Priyantha (2005) with their limited range, the Global Positioning System (GPS) which does not work indoors, to name a few and their respective shortcomings. However, a framework, which has become a common standard base, is the inertial estimation framework, often a part of Inertial Navigation Systems, has been subject of research for en extended period of time with recognized works such as the ones in Titterton and Weston (2004); Woodman (2007); Grewal et al. (2007).

Towards the following trend, an area which is heavily based on inertial estimation and is currently under intense research is the Visual Inertial Odometry (VIO), which is

Fig. 1. A photo of the Ascending Technologies Neo hexacopter with the UWB hardware attached as used in the experiments.

based on combining a camera and an Inertial Measurement Unit (IMU) that leverages the high bandwidth of the IMU, *i.e.* accelerometers and gyroscopes, with the high local stability of a camera and visual features. These systems, while having impressive local accuracy Li et al. (2014); Bloesch et al. (2015); Mur-Artal et al. (2015), drift over time on a global scale, when detecting new and discarding old features. To correct for this drift, either a larger map is needed, which eventually reaches its limit due to storage or processing constraints, or a system which can provide corrections on a larger scale is necessary – corrections which we will explore in the sequel.

In parallel to these developments, due to the recent changes in Radio Frequency (RF) regulations, IEEE Standard 802.15.4-2011 (2011), a technology previously used only in military and radar applications, have been stan-

dardized – namely the Ultra WideBand (UWB), which is an RF technology that operates on a wide band of frequencies, rather than utilizing carrier waves as most communication does today, as will be discussed in the sequel. The main point with this technology is its ability to accurately time stamp multiple messages, allowing the Time of Flight (TOF) of the message to be calculated, which, when multiple transceivers are utilized, it can be seen as a local GPS system.

A pioneering work, in the area of UWB, was the one in Mueller et al. (2015) that performed state estimation of a quadrotor helicopter using its dynamic model together with an IMU and UWB distance measurements to observe its state. This included estimating the thrust constant for predicting its accelerations, while the established method had two drawbacks: a) only forces which are modeled could be considered, which implies that disturbances, such as wind, can cause large errors in the estimation, and b) the IMU measurements were considered as measurements from the Kalman Filter's point of view, forcing the filter to perform full measurement updates at IMU rates, which was 1 kHz.

The specific contribution and impact of this paper stems from the aim to improve the previous scheme with the following novelties: 1) by establishing a generic localization system based on inertial odometry and UWB, which does need the dynamics of the system, allowing it to be used in a multitude of application areas (generalized form), 2) modeling the translation from IMU to the center of antenna, and 3) having the ability to select the optimal distance measurements in order to minimize the system's covariance, while simultaneously minimizing the RF air utilization. The efficacy of the proposed generalized UWB enabled scheme will be demonstrated during demanding indoor flying tests with an hexacopter Unmanned Aerial Vehicle (UAV).

The rest of the paper is structured as it follows. In Section 2 the general theory of operation of the IMU and UWB system is presented, while in Section 3 the Inertial Estimation Framework is described. Finally in Section 4 experimental setup and results are presented with Conclusions being drawn in Section 5.

Nomenclature Scalars are defined as non-bold characters such as s or S, while vectors are bold lower-case letters such as $\boldsymbol{v}$ and finally matrices are bold upper-case letters such as $\boldsymbol{A}$.

The coordinate frames in this paper are defined as: 1) the world frame $\mathcal{W}$, 2) the UWB network frame $\mathcal{U}$ and 3) the IMU frame $\mathcal{I}$, where, *e.g.* $\boldsymbol{v}_\mathcal{W}$ is a vector in the world frame, as will be presented in Figure 8.

The quaternions in this paper are the passive Hamilton quaternion of unit length (see Kuipers (1998) for details), which implies that the quaternion $\boldsymbol{q}_{\mathcal{GL}}$ is a Local-to-Global rotation made in a right-handed coordinate system, while the corresponding rotation matrix is defined as $\boldsymbol{R}(\boldsymbol{q}_{\mathcal{GL}}) = \boldsymbol{R}_{\mathcal{GL}}$, implying $\boldsymbol{v}_\mathcal{G} = \boldsymbol{R}_{\mathcal{GL}}\boldsymbol{v}_\mathcal{L}$.

When referring to a UWB network, an *anchor* is a UWB transceiver that is stationary with known relative position to the other anchors in the network, while a *node* is a UWB transceiver that is moving which we want to estimate.

2. THEORY OF OPERATION

2.1 Inertial Measurement Unit

The utilized sensor is the one of the Micro-Electro-Mechanical Systems (MEMS) IMU, more specifically the MEMS gyroscope and accelerometer due to their small size, low cost and high availability. These sensors do however suffer from several non-ideal effects, such as gain, bias and axis misalignment errors, which are a combination off static and varying errors. For the accelerometer and gyroscope these errors can be modeled in the standard way as in Titterton and Weston (2004); Li et al. (2014). More specifically, in case of the accelerometer the errors can be expressed as:

$$\boldsymbol{a}_m = \boldsymbol{T}_a \boldsymbol{a}_s + \boldsymbol{a}_b + \boldsymbol{a}_n \tag{1}$$
$$\boldsymbol{a}_s = \boldsymbol{a}_{true} + \boldsymbol{R}_{\mathcal{WI}}^T \boldsymbol{g}_\mathcal{W} \tag{2}$$
$$\dot{\boldsymbol{a}}_b = \boldsymbol{a}_{bn}, \tag{3}$$

where $\boldsymbol{T}_a \in \mathbb{R}^{3\times3}$ is the transform matrix containing gain and misalignment errors, $\boldsymbol{a}_b \in \mathbb{R}^3$ is the accelerometer bias, $\boldsymbol{a}_n \sim \mathcal{N}(0, \sigma_{an}^2)$, $\boldsymbol{a}_{bn} \sim \mathcal{N}(0, \sigma_{abn}^2)$ denote the measurement and driving bias noise respectively, and $\boldsymbol{R}_{\mathcal{WI}}^T \boldsymbol{g}_\mathcal{W} \in \mathbb{R}^3$ is the gravity vector in the IMU frame. While for the gyroscope, the errors are defined as following:

$$\boldsymbol{\omega}_m = \boldsymbol{T}_\omega \boldsymbol{\omega}_{true} + \boldsymbol{T}_{\omega a} \boldsymbol{a}_s + \boldsymbol{\omega}_b + \boldsymbol{\omega}_n \tag{4}$$
$$\dot{\boldsymbol{\omega}}_b = \boldsymbol{\omega}_{bn}, \tag{5}$$

where $\boldsymbol{T}_\omega \in \mathbb{R}^{3\times3}$ is the transform matrix containing gain and misalignment errors, $\boldsymbol{T}_{\omega a} \in \mathbb{R}^{3\times3}$ is the transform matrix containing acceleration sensitivity, $\boldsymbol{\omega}_n \sim \mathcal{N}(0, \sigma_{\omega n}^2)$, $\boldsymbol{\omega}_{bn} \sim \mathcal{N}(0, \sigma_{\omega bn}^2)$ denotes measurement and driving bias noise respectively.

2.2 Ultra WideBand Distance Measurements

Operating principle: UWB RF communication is based on using a wide band of the RF spectrum, rather than a single frequency as carrier wave radio does, which has the temporal representation of a pulse and as a result is sometimes referred to as a pulse radio. Due to the high center frequency (3.1 to 4.8 GHz and 6.0 to 10.6 GHz) and the spectral width of the pulse (499.2 MHz to 1331.2 MHz), as specified in Decawave (2015); IEEE Standard 802.15.4-2011 (2011), the pulses have very good spatial resolution, which makes them ideal for time stamping RF packets, referred to as messages, with high accuracy. This property of accurate time stamps (within the message), together with good reference clocks, give the ability to estimate the distance between two transceivers by exchanging 2 or more packets and thus it could be considered that the distance estimation is a bi product of the communication.

Furthermore, one major drawback of carrier wave based radio is the problem of multipathing, where the carrier wave forms destructive interference with itself, effectively reducing the received signal strength. This is a problem that is severely mitigated in the UWB radio, where the spatial length of each pulse is small enough for each pulse to be detected uniquely and this allows the receiver to reconstruct the pulse from multiple reflections. In a sense,

the more reflections there are available, the stronger the received signal is.

Distance measurements: As hinted in the prequel, the estimation of distance between two transceivers is the bi product of multiple exchange of messages between the two transceivers as presented in Figure 2. This is made possible by sending a message that at a specific time instance can be identified and time stamped, which is represented by the thick line in each message box in the Figure, and by scheduling messages in the future to know at which time the message was sent. The worst case time for each message, in the system presented, is 116 us, with a delay between messages of 300 us – providing an entire sequence in approximately 1360 us, including a fourth message containing the distance estimate, which gives a maximum rate of 733 Hz. However, as specified in ETSI (2016), the maximum allowed air time is 5 % of every second, making the legal limit of the system 108 Hz.
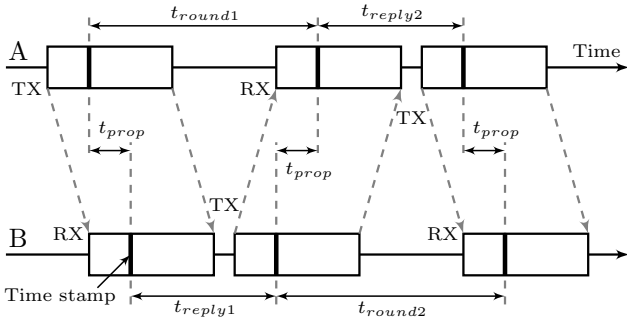

Fig. 2. A decryption of an entire ranging sequence, where each box represents an UWB packet, while the thick lines inside are the point of time stamp extraction.

The time of flight or, as it is also referred to, the propagation time can then be estimated based on Decawave (2015) as it follows:

$$\hat{t}_{prop} = \frac{t_{round1} \cdot t_{round2} - t_{reply1} \cdot t_{reply2}}{t_{round1} + t_{round2} + t_{reply1} + t_{reply2}}, \quad (6)$$

while multiplication with the speed of light in air gives the estimated distance in meters:

$$d_m = \hat{t}_{prop} c_{air}. \quad (7)$$

This estimate is however not without fault, since two additional sources of error exist as:

$$d_m = d_{true} + d_b + d_n \quad (8)$$

with $d_b \in \mathbb{R}$ being a bias on the measurement, being introduced from the antenna delay, which is the time it takes for the signal to propagate from the antenna to the receiver, and a noise term $d_n \sim \mathcal{N}(0, \sigma_{UWB}^2)$ which has been found to be $\sigma_{UWB} \approx 21.4$ mm for the system in this paper, as presented in Figure 3.

Outliers: In distance estimation one of the most common source of errors is when the first path is blocked and some later path, *i.e.* a reflection, is detected as first path, as depicted in Figure 4, which generates an outlier. At these situations it's important to note, as this effect is frequently occurring, the estimation scheme using this information needs to employ some form of outlier rejection or use the notion, that an outlier is always longer than the true
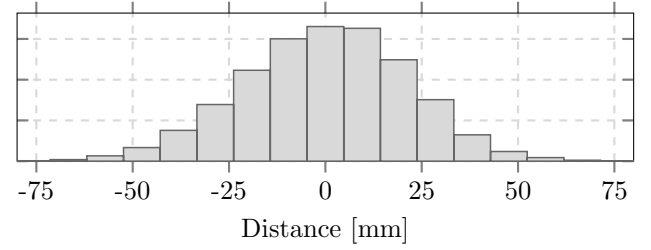

Fig. 3. Histogram over 195 000 distance measurements where the mean has been removed.

distance, or $d_{outlier} > d_{true}$. As it will be presented in the sequel, we have opted for the use of outlier rejection.
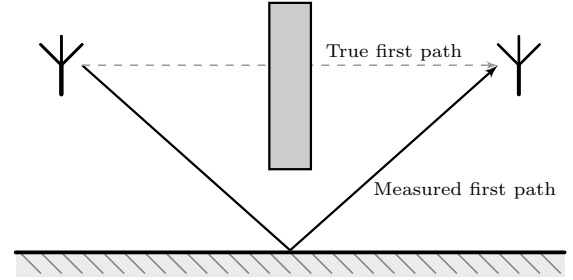

Fig. 4. An example of outliers generated via reflections.

2.3 Ultra WideBand Measurement Schemes

Cyclic measurements: The simplest, and most naive, scheme is the cyclic measurement scheme, as depicted in Figure 5, where all UWB anchors in range are kept in a list that it is iterated over at a fixed rate. This method, while being simple, does not have any more appealing qualities as it can do a lot distance measurements that do not have significant impact on the system's covariance, and since it runs at a fixed rate it can potentially waste precious air time of the network.
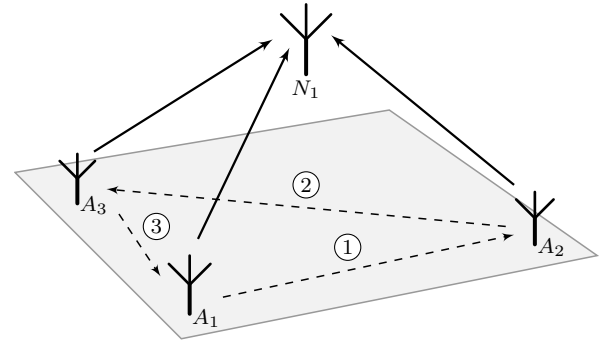

Fig. 5. Cyclic measurement scheme, where the anchor to measure is rotated among the anchors in range.

Stochastic events: An arguably better approach would be to examine the covariance of the system and put specifications on the allowed uncertainty with a threshold σ_{th}. This can be done by spectral decomposition of the estimated position's covariance matrix $\boldsymbol{P}_{\hat{\boldsymbol{p}}}$, through Principal Component Analysis (PCA):

$$\boldsymbol{P}_{\hat{\boldsymbol{p}}} = \lambda_1 \boldsymbol{c}_1 \boldsymbol{c}_1^T + \lambda_2 \boldsymbol{c}_2 \boldsymbol{c}_2^T + \lambda_3 \boldsymbol{c}_3 \boldsymbol{c}_3^T, \quad (9)$$

where $\lambda_n \in \mathbb{R}_+$ are the eigenvalues in decreasing order of magnitude and $\boldsymbol{c}_n \in \mathbb{S}^2$ are the corresponding eigenvectors. From the decomposition we extract the principal

component of the covariance matrix and its corresponding variance, which is compared to the threshold and if a measurement is needed ($\sigma_{th}^2 < \lambda_1$), the UWB anchor that will minimize the system's uncertainty is chosen, as depicted in Figure 6. Since distance measurements only can give corrections along the vector, which goes through both the anchor's and the node's position, the measurement that aligns the most with the covariance's principal axis will provide the best achievable measurement to minimize the uncertainty. The solution to this problem can be cast as the following optimization problem:

$$\underset{A_m}{\text{maximize}} \left\| \boldsymbol{c}_1 \cdot \left(\frac{\boldsymbol{p}_N - \boldsymbol{p}_{A_m}}{\|\boldsymbol{p}_N - \boldsymbol{p}_{A_m}\|_2} \right) \right\| \tag{10}$$

$$\text{subject to} \quad \|\boldsymbol{p}_N - \boldsymbol{p}_{A_m}\|_2 < d_{max},$$

where A_m is the current UWB anchor under examination and d_{max} is the maximum range of the node. This mixed-integer optimization problem is solved through exhaustive search, since the search space is growing linearly with the number of UWB anchors. It should also be noted that more terms can be added to this cost function that penalizes failed ranging or distance to anchors, however this will not examined further in this paper.
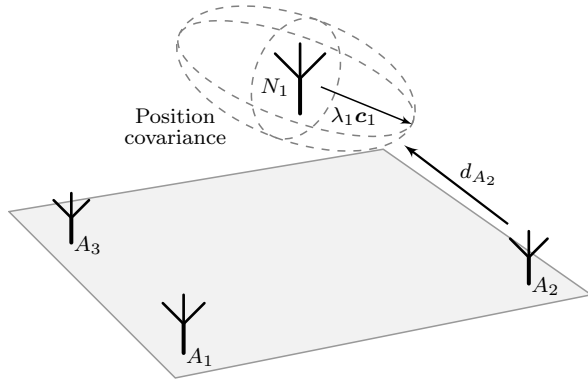

Fig. 6. The covariance ellipsoid of the position states is used to generate events which initiate measurements to the optimal anchor.

2.4 Anchor placement for unique solutions

For performing localization in 3 dimensions, a minimum number of 3 UWB anchors are required, however the solution is then not unique as presented in Figure 7. For a unique solution there must exist at least one extra UWB anchor, A_4, which is not in the plane spanned by the first three nodes, as presented in Theorem 1.

Theorem 1. For the localization to be unique, let $S = \{\boldsymbol{p}_{A_2} - \boldsymbol{p}_{A_1}, \ \boldsymbol{p}_{A_3} - \boldsymbol{p}_{A_1}\}$ be the set of vectors, which span a plane by the positions of anchors A_1, A_2 and A_3, then the forth anchor must then be placed so $\boldsymbol{p}_{A_4} - \boldsymbol{p}_{A_1} \notin \text{span}(S)$.

Proof 1. Given the anchors' positions in the following canonical form:

$$\boldsymbol{p}_{A_1} = \begin{bmatrix} 0 \\ 0 \\ 0 \end{bmatrix} \ \boldsymbol{p}_{A_2} = \begin{bmatrix} x_0 \\ 0 \\ 0 \end{bmatrix} \ \boldsymbol{p}_{A_3} = \begin{bmatrix} x_1 \\ y_1 \\ 0 \end{bmatrix} \ \boldsymbol{p}_{A_4} = \begin{bmatrix} x_2 \\ y_2 \\ z_2 \end{bmatrix}, \tag{11}$$

with $x_0, y_1, z_2 \neq 0$, which can be constructed from a QR decomposition, and the node's position as:

$$\boldsymbol{p}_N = [x_n \ y_n \ z_n]^T, \tag{12}$$

we can solve for $\boldsymbol{p}_N$ using the corresponding distances:

$$\|\boldsymbol{p}_{A_1} - \boldsymbol{p}_N\|_2 = d_{A_1}, \tag{13}$$
$$\|\boldsymbol{p}_{A_2} - \boldsymbol{p}_N\|_2 = d_{A_2}, \tag{14}$$
$$\|\boldsymbol{p}_{A_3} - \boldsymbol{p}_N\|_2 = d_{A_3}, \tag{15}$$
$$\|\boldsymbol{p}_{A_4} - \boldsymbol{p}_N\|_2 = d_{A_4}. \tag{16}$$

Each corresponding solution, after squaring both sides, substitution and simplification, becomes:

$$z_n^2 = d_{A_1}^2 - x_n^2 - y_n^2, \tag{17}$$
$$x_n = \frac{x_0^2 + d_{A_1}^2 - d_{A_2}^2}{2x_0}, \tag{18}$$
$$y_n = \frac{x_1^2 + y_1^2 - 2x_1 x_n + d_{A_1}^2 - d_{A_3}^2}{2y_1}, \tag{19}$$
$$z_n = \frac{x_2^2 + y_2^2 + z_2^2 - 2x_2 x_n - 2y_2 y_n + d_{A_1}^2 - d_{A_4}^2}{2z_2}, \tag{20}$$

where equation (20), solved from equation (16), gives the uniqueness in the z-axis. Without this extra equation, or $z_2 = 0$, only equation (17) exists which gives both a positive and a negative solution for z_n. ∎
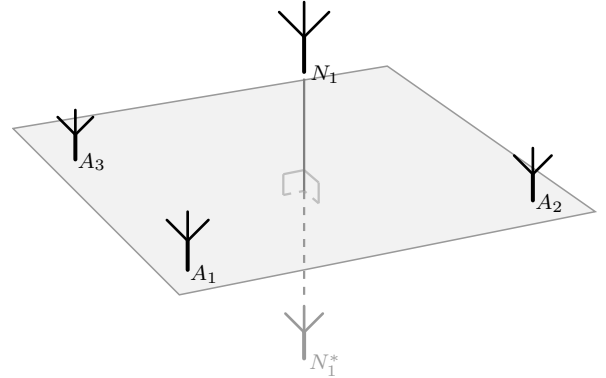

Fig. 7. When using only three anchors the mirroring problem occurs, where the out-of-plane coordinate has two solutions.

3. INERTIAL ESTIMATION FRAMEWORK

For estimating the inertial odometry, including pose, twist and biases of the IMU, using corrections from the UWB network, the standard kinematic state vector Sola (2016); Trawny and Roumeliotis (2005), with the work by Sola being the most up to date, is employed:

$$\hat{\boldsymbol{x}} = \begin{bmatrix} \boldsymbol{p}_{\mathcal{U}}^T & \boldsymbol{v}_{\mathcal{U}}^T & \boldsymbol{q}_{\mathcal{UI}}^T & \boldsymbol{b}_\omega^T & \boldsymbol{b}_a^T \end{bmatrix}^T \in \mathbb{R}^{16 \times 16}, \tag{21}$$

where $\boldsymbol{p}_{\mathcal{U}}, \boldsymbol{v}_{\mathcal{U}} \in \mathbb{R}^3$ is the position and velocity respectively in the frame of the UWB network, $\boldsymbol{q}_{\mathcal{UI}} \in \mathbb{SO}(3)$ is the attitude quaternion from the IMU frame to the frame of the UWB network, while $\boldsymbol{b}_\omega, \boldsymbol{b}_a \in \mathbb{R}^3$ are the gyroscope's and accelerometer's biases respectively, while the kinematics have the following continuous time dynamics:

$$\dot{\boldsymbol{p}}_{\mathcal{U}} = \boldsymbol{v}_{\mathcal{U}} \tag{22}$$
$$\dot{\boldsymbol{v}}_{\mathcal{U}} = \boldsymbol{R}(\boldsymbol{q}_{\mathcal{UI}})(\boldsymbol{a}_m - \boldsymbol{b}_a - \boldsymbol{a}_n) + \boldsymbol{R}_{\mathcal{WU}}^T \boldsymbol{g}_{\mathcal{W}} \tag{23}$$
$$\dot{\boldsymbol{q}}_{\mathcal{UI}} = \frac{1}{2} \, \boldsymbol{q}_{\mathcal{UI}} \otimes (\boldsymbol{\omega}_m - \boldsymbol{b}_\omega - \boldsymbol{\omega}_n) \tag{24}$$
$$\dot{\boldsymbol{b}}_\omega = \boldsymbol{\omega}_{bn} \tag{25}$$
$$\dot{\boldsymbol{b}}_a = \boldsymbol{a}_{bn}, \tag{26}$$

where $\boldsymbol{a}_m, \boldsymbol{\omega}_m \in \mathbb{R}^3$ are the measured acceleration [m/s²] and angular rate [rad/s] respectively, while $\boldsymbol{a}_n, \boldsymbol{a}_{bn}, \boldsymbol{\omega}_n, \boldsymbol{\omega}_{bn}$ are the noise and driving bias noise for the accelerometer and gyroscope respectively, from Section 2.1. However, in the inertial estimation framework the accelerometer and gyroscope are considered inputs to the estimation (Sola (2016); Trawny and Roumeliotis (2005)) as:

$$\boldsymbol{u} = \begin{bmatrix} \boldsymbol{a}_m^T & \boldsymbol{\omega}_m^T \end{bmatrix}^T, \tag{27}$$

rather than measurements, as the nominal state is driven by the IMU. An overview of the different coordinate frames utilized are depicted in Figure 8.
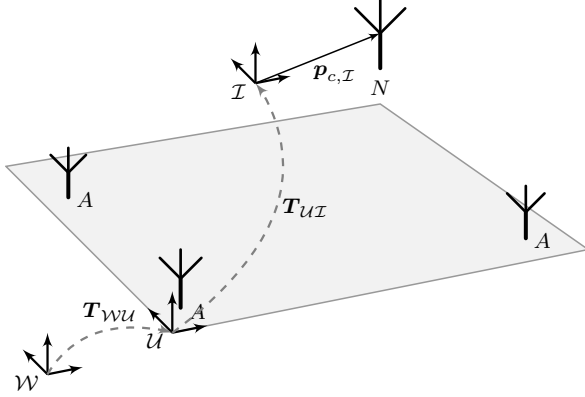

Fig. 8. Description of coordinate frames utilized, the world $\mathcal{W}$, UWB network $\mathcal{U}$ and IMU $\mathcal{I}$ frame, where $\boldsymbol{T}$ is the transform between frames as indicated by the arrows.

3.1 Error-state formulation

As described in the previous works by Trawny and Roumeliotis (2005) and Sola (2016), the state is rewritten as a nominal part and an error part ($\hat{\boldsymbol{x}} = \boldsymbol{x}_n \oplus \delta\boldsymbol{x}$), where all large signal changes, *i.e.* IMU measurements, are integrated in the nominal state while the errors are observed through measurements. This has the distinct advantage of a) being a *minimal* representation of the state and b) the slow errors are always integrated in the nominal state, keeping the error state *very close* or *equal* to zero. This gives the following error state vector:

$$\delta\boldsymbol{x} = \begin{bmatrix} \delta\boldsymbol{p}^T & \delta\boldsymbol{v}^T & \delta\boldsymbol{\theta}^T & \delta\boldsymbol{b}_\omega^T & \delta\boldsymbol{b}_a^T \end{bmatrix}^T \in \mathbb{R}^{15 \times 15}, \tag{28}$$

where

$$\delta\boldsymbol{q} \approx \begin{bmatrix} 1, & \frac{1}{2}\delta\boldsymbol{\theta}^T \end{bmatrix}^T, \tag{29}$$

produces the minimal state representation by using the small angle approximation of the error quaternion. The following error dynamics arises from the kinematic state dynamics, and are included for clarity and completeness of presentation:

$$\dot{\delta\boldsymbol{p}} = \delta\boldsymbol{v} \tag{30}$$

$$\dot{\delta\boldsymbol{v}} = -\boldsymbol{R}_{\mathcal{U}\mathcal{I}} \left([\boldsymbol{a}_m - \delta\boldsymbol{b}_a]_\times \delta\boldsymbol{\theta} + \delta\boldsymbol{b}_a + \boldsymbol{a}_n \right) \tag{31}$$

$$\dot{\delta\boldsymbol{\theta}} = -[\boldsymbol{\omega}_m - \delta\boldsymbol{b}_\omega]_\times \delta\boldsymbol{\theta} - \delta\boldsymbol{b}_\omega - \boldsymbol{\omega}_n \tag{32}$$

$$\dot{\delta\boldsymbol{b}}_\omega = \boldsymbol{\omega}_{bn} \tag{33}$$

$$\dot{\delta\boldsymbol{b}}_a = \boldsymbol{a}_{bn}, \tag{34}$$

where $[\boldsymbol{a}]_\times \boldsymbol{b} = \boldsymbol{a} \times \boldsymbol{b}$ is the skew-symmetric cross product matrix.

An overview of the Error-state Kalman Filter (ESKF) for inertial odometry with UWB corrections is presented in Figure 9, where the *State Update*-block is responsible for the large signal integration while also integrating the error corrections, while the ESKF performs the error estimation, measurement and covariance updates.
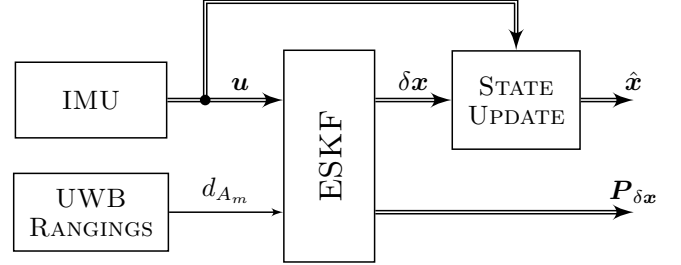

Fig. 9. An overview of the error-state Kalman Filter utilized in the experiments.

3.2 Measurement injection

For observing the error-states through the UWB distance measurements, the predicted measurement is written as a function of the nominal state and the error-state, while also including the distance from IMU to the center of the UWB antenna as:

$$d_{A_m} = \left\| (\boldsymbol{p}_n + \delta\boldsymbol{p}) + \boldsymbol{R}(\boldsymbol{q}_n \otimes \delta\boldsymbol{q})\boldsymbol{p}_{c,\mathcal{I}} - \boldsymbol{p}_{A_m} \right\|_2. \tag{35}$$

For deriving the measurement Jacobian, the following rewrite of equation (35) is performed:

$$d_{A_m} = \sqrt{g(\delta\boldsymbol{p}, \delta\boldsymbol{\theta})} \tag{36}$$

$$g(\delta\boldsymbol{p}, \delta\boldsymbol{\theta}) = \boldsymbol{h}(\delta\boldsymbol{p}, \delta\boldsymbol{\theta})^T \boldsymbol{h}(\delta\boldsymbol{p}, \delta\boldsymbol{\theta}) \tag{37}$$

$$\boldsymbol{h}(\delta\boldsymbol{p}, \delta\boldsymbol{\theta}) = (\boldsymbol{p}_n + \delta\boldsymbol{p}) + \boldsymbol{R}(\boldsymbol{q}_n \otimes \delta\boldsymbol{q}(\delta\boldsymbol{\theta}))\boldsymbol{p}_{c,\mathcal{I}} - \boldsymbol{p}_{A_m} \tag{38}$$

and for extracting each contribution, the chain rule is applied (with some abuse of notation):

$$\frac{\partial d_{A_m}}{\partial \delta\boldsymbol{p}} = \frac{\partial d_{A_m}}{\partial g} \frac{\partial g}{\partial \boldsymbol{h}} \frac{\partial \boldsymbol{h}}{\partial \delta\boldsymbol{p}} \tag{39}$$

$$\frac{\partial d_{A_m}}{\partial \delta\boldsymbol{\theta}} = \frac{\partial d_{A_m}}{\partial g} \frac{\partial g}{\partial \boldsymbol{h}} \frac{\partial \boldsymbol{h}}{\partial \delta\boldsymbol{\theta}}, \tag{40}$$

in which each contribution is:

$$\frac{\partial d_{A_m}}{\partial g} = \frac{1}{2d_{A_m}} \tag{41}$$

$$\frac{\partial g}{\partial \boldsymbol{h}} = 2\boldsymbol{h}^T \tag{42}$$

$$\frac{\partial \boldsymbol{h}}{\partial \delta\boldsymbol{p}} = \boldsymbol{I}_{3\times 3} \tag{43}$$

$$\frac{\partial \boldsymbol{h}}{\partial \delta\boldsymbol{\theta}} = -[\boldsymbol{R}(\boldsymbol{q}_n)\boldsymbol{p}_{c,\mathcal{I}}]_\times \tag{44}$$

where equation (44) were derived by Sola (2016), where the corresponding details of the derivation can be found.

3.3 Outlier rejection

As discussed in Section 2.2.3, the UWB distance measurements are plagued with outliers when the first path is not detected, however the characteristics of the outliers are

quite simple as $d_{outlier} > d_{true}$, and most importantly, it was found through experiments that:

$$\|d_{outlier} - d_{true}\|_2 \gg \sigma_{UWB}, \tag{45}$$

which allows for simple threshold removal by utilizing Mahalanobis distance from Mahalanobis (1936).

4. EXPERIMENTAL EVALUATION

4.1 Hardware

The UWB hardware employed was developed and manufactured at Luleå University of Technology, based on the Decawave DW1000 chipset, as depicted in Figure 10 and 1. The UWB node includes on board processing in the form of an Cortex-M4F Central Processing Unit (CPU), together with multiple communication peripherals, including USB and serial port. Moreover, the IMU used in the experiments is an *consumer grade* IMU (Invensense MPU-6000), sampling at 220 Hz, to emphasize the robustness of the proposed estimation scheme, while also emphasizing the *low cost* of the solution – making it ideal for general low-cost localization.

Fig. 10. A photo of the UWB hardware used in the experiments, developed at Luleå University of Technology.

4.2 Anchor placement

For the experiments, the anchors were placed as depicted in Figure 11, where the box in the center is the $5 \times 5 \times 2.8$ m flying volume. The exact position of each anchor is presented in Table 1, and were measured using the Vicon motion capture system.
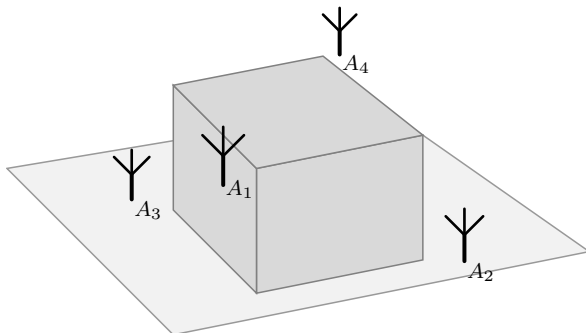

Fig. 11. A sketch over the flying volume and how the anchors were placed in relation to it.

Table 1. Placement of the anchors during the experiments.

	x [m]	**y** [m]	**z** [m]
Anchor 1	-4.12	-3.67	2.72
Anchor 2	2.45	-2.70	0.063
Anchor 3	-2.43	3.07	0.075
Anchor 4	3.65	2.42	2.65

4.3 Error-state Kalman Filter implementation

For experimental evaluation a specific implementation of the ESKF is needed, and in this work we opted for the use of the Multi Sensor Fusion (MSF) package by Lynen et al. (2013), because of its high flexibility, ease of adding new measurement functions, and included Mahalanobis distance outlier rejector.

4.4 Practical considerations

From equation (23) it is apparent that the gravitational vector needs to be in the UWB network's frame of reference, for this to hold in the experiments the network's base plane has manually been aligned with the gravitational vector providing: $z_{\mathcal{U}} \parallel g_{\mathcal{W}} \rightarrow g_{\mathcal{W}} = g_{\mathcal{U}}$.

4.5 Tracking results

For evaluating the proposed system, it was evaluated in four scenarios. One based on the naive, cyclic ranging scheme, two based on stochastic events with different thresholds, and one final which shows the system converging in yaw even though it is never directly observed. All experiments consists of a Ascending Technologies Neo hexacopter being fitted with one UWB node, that was flown with square and diagonal trajectories within the flying arena of the Field Robotics Lab (FROST). The flying arena is equipped with a Vicon motion capture system, consisting of 20 Vicon T40s cameras, which were used as ground truth reference at 100 Hz.

Cyclic scheme: For the cyclic scheme the rotation rate was set to the standard rate of the system, being 80 Hz, while the results are depicted in the first column of Figure 12 with corresponding RMSE in Table 2. As can be seen in the Figure, the system performs well without spurious event and with good convergence and tracking.

Event scheme: The stochastic event based measurement system was evaluated with two thresholds, $\sigma_{th} = 0.07$ m and $\sigma_{th} = 0.15$ m to show the difference in sampling rate and accuracy. As depicted in the second column of Figure 12, the experiment with the tighter bound shows generally the same uncertainty as the fixed rate system, however at almost half the sampling rate (45.5 Hz mean) as depicted in the first sub-figure of Figure 13 – clearly showing the efficacy of the proposed system. While as an indicative example the looser bound, depicted in the third column of Figure 12, still performs well with a mean sampling rate of 8.8 Hz, depicted in the second sub-figure of Figure 13. It's important to note how the sampling rate is adapting over time in Figure 13, in order to adhere to the variance specifications, where the quality of the IMU
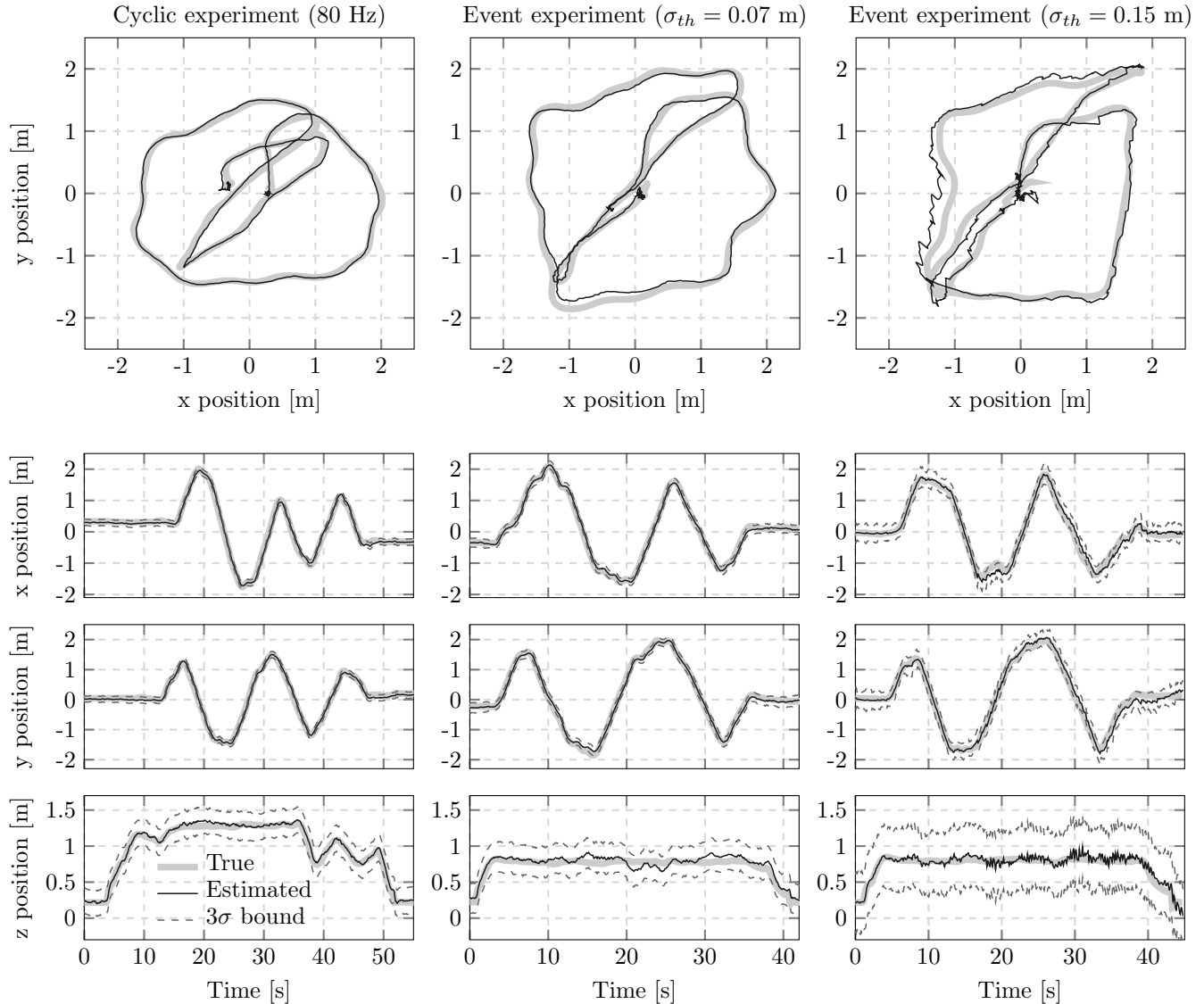
Fig. 12. Results from all experiments, where each column is one experiment and the first row being an XY graph, while each following row are the details for the *x*- *y*- and *z*-axis respectively, including 3σ bounds.

(*i.e.* IMU noise), the geometry, and density of the UWB network will determine the sampling rate of the system.

In contrast to Mueller et al. (2015), the UWB sampling rates of this scheme are within the maximum air time as discussed in Section 2.2.2, while also utilizing much lower IMU rates of 220 Hz vs. 1 kHz.

Yaw convergence: Finally, an experiment was performed to evaluate the convergence of yaw when initialized with a large error, as depicted in Figure 14. The hexacopter was moved around within the flying arena, and even though the system cannot observe the yaw directly it does converge. This comes from equation (31), which observes the yaw error if there are accelerations in the *x*- or *y*-axis of the UWB network's frame of reference, suggesting that *e.g.* magnetometers, which are sensitive to errors Fresk et al. (2016), can be excluded – reducing complexity while retaining performance.
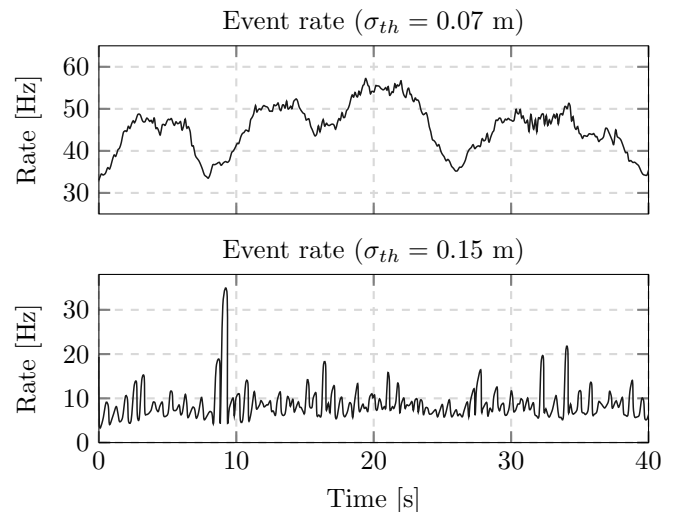

Fig. 13. An overview of how the measurement rate changes over time for the two event based experiments.
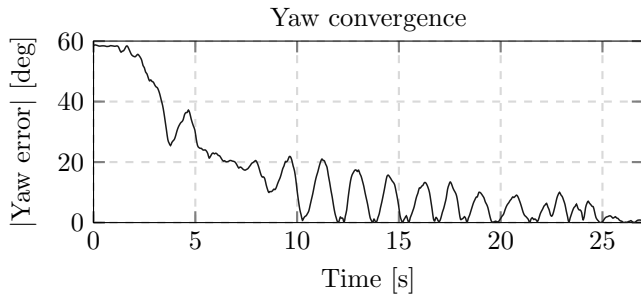
Yaw convergence

Fig. 14. Convergence of the yaw error during the yaw experiment.

Table 2. Estimation RMSE for all experiments.

Axis	Cyclic	Event $\sigma_{th} = 0.07$ m	Event $\sigma_{th} = 0.15$ m
Roll [deg]	1.60	2.08	1.93
Pitch [deg]	1.60	1.69	1.75
Yaw [deg]	5.49	6.50	4.94
X [m]	0.064	0.069	0.11
Y [m]	0.054	0.072	0.12
Z [m]	0.035	0.063	0.083

5. CONCLUSIONS

In this paper a novel generic localization system based on IMU driven kinematics, through an ESKF, with UWB corrections has been presented. The localization system was evaluated in two forms, one cyclic measurement scheme and an stochastic event based scheme, where the later has the strong merit of minimizing the measurement rate needed to keep variance specifications. This allows the system to operate within current RF regulations, allowing more systems to run in parallel. The system has been evaluated in extended experimental evaluation on an hexacopter UAV, clearly showing the efficacy of the proposed scheme.

REFERENCES

Bloesch, M., Omari, S., Hutter, M., and Siegwart, R. (2015). Robust visual inertial odometry using a direct ekf-based approach. In *Intelligent Robots and Systems (IROS), 2015 IEEE/RSJ International Conference on*, 298–304. IEEE.

Decawave (2015). DW1000 User Manual v2.10. URL http://www.decawave.com/.

ETSI (2016). ETSI TR 103 181-3 Part 3: Worldwide UWB regulations between 3.1 and 10.6 GHz. URL http://www.etsi.org/.

Fresk, E., Nikolakopoulos, G., and Gustafsson, T. (2016). A Generalized Reduced-Complexity Inertial Navigation System for Unmanned Aerial Vehicles. *IEEE Transactions on Control Systems Technology*, PP(99), 1–16.

Grewal, M.S., Weill, L.R., and Andrews, A.P. (2007). *Global positioning systems, inertial navigation, and integration.* John Wiley & Sons.

IEEE Standard 802.15.4-2011 (2011). IEEE Standard for Local and metropolitan area networks– Part 15.4: Low-Rate Wireless Personal Area Networks (LR-WPANs). *IEEE Standard 802.15.4-2011 (Revision of IEEE Standard 802.15.4-2006)*, 1–314. doi: 10.1109/IEEESTD.2011.6012487.

Kuipers, J.B. (1998). *Quaternions and Rotation Sequences.*

Li, M., Yu, H., Zheng, X., and Mourikis, A.I. (2014). High-fidelity sensor modeling and self-calibration in vision-aided inertial navigation. In *2014 IEEE International Conference on Robotics and Automation (ICRA)*, 409–416. IEEE.

Lynen, S., Achtelik, M., Weiss, S., Chli, M., and Siegwart, R. (2013). A Robust and Modular Multi-Sensor Fusion Approach Applied to MAV Navigation. In *Proc. of the IEEE/RSJ Conference on Intelligent Robots and Systems (IROS)*.

Mahalanobis, P.C. (1936). On the generalized distance in statistics. *Proceedings of the National Institute of Sciences (Calcutta)*, 2, 49–55.

Mellinger, D. and Kumar, V. (2011). Minimum snap trajectory generation and control for quadrotors. In *Robotics and Automation (ICRA), 2011 IEEE International Conference on*, 2520–2525. IEEE.

Mueller, M.W., Hamer, M., and D'Andrea, R. (2015). Fusing ultra-wideband range measurements with accelerometers and rate gyroscopes for quadrocopter state estimation. In *2015 IEEE International Conference on Robotics and Automation (ICRA)*, 1730–1736. IEEE.

Mur-Artal, R., Montiel, J., and Tardós, J.D. (2015). ORB-SLAM: a versatile and accurate monocular slam system. *IEEE Transactions on Robotics*, 31(5), 1147–1163.

Newman, P., Cole, D., and Ho, K. (2006). Outdoor slam using visual appearance and laser ranging. In *Proceedings 2006 IEEE International Conference on Robotics and Automation, 2006. ICRA 2006.*, 1180–1187. IEEE.

Priyantha, N.B. (2005). *The cricket indoor location system.* Ph.D. thesis, Massachusetts Institute of Technology.

Sola, J. (2016). Quaternion kinematics for the error-state KF. *Laboratoire d'Analyse et d'Architecture des Systemes-Centre national de la recherche scientifique (LAAS-CNRS), Toulouse, France, Tech. Rep.*

Tardós, J.D., Neira, J., Newman, P.M., and Leonard, J.J. (2002). Robust mapping and localization in indoor environments using sonar data. *The International Journal of Robotics Research*, 21(4), 311–330.

Titterton, D. and Weston, J.L. (2004). *Strapdown inertial navigation technology*, volume 17. IET.

Trawny, N. and Roumeliotis, S.I. (2005). Indirect Kalman Filter for 3D Attitude Estimation. Technical report, Department of Computer Science & Engineering.

Woodman, O.J. (2007). An introduction to inertial navigation. *University of Cambridge, Computer Laboratory, Tech. Rep. UCAMCL-TR-696*, 14, 15.

Zhao, H., Chiba, M., Shibasaki, R., Shao, X., Cui, J., and Zha, H. (2008). Slam in a dynamic large outdoor environment using a laser scanner. In *Robotics and Automation, 2008. ICRA 2008. IEEE International Conference on*, 1455–1462. IEEE.